



Advanced FE model validation of cold-forming process using DIC: Air bending of high strength steel

S. Gothivarekar¹ · S. Coppieters¹ · A. Van de Velde¹ · D. Debruyne¹

Received: 29 July 2019 / Accepted: 9 January 2020 / Published online: 4 March 2020
© Springer-Verlag France SAS, part of Springer Nature 2020

Abstract

Recent advances in mechanical and civil engineering are noticed in many innovative designs that frequently employ cold-formed High Strength Steels (HSS). Typical mobile cranes benefit from the advanced properties of these steel grades in a bent configuration. Here, the majority of load-carrying members are produced through cold-bending and subsequent welding procedures. These cold-forming processes induce residual stresses and strains that must be considered when assessing the structural integrity and service life of bent sections in an assembly. Finite Element Analysis (FEA) offers a unique solution here to reproduce the bending process accurately. However, this analysis must be verified using representative validation methods. If these methods remain scarce, basic or incomplete, the credibility of a sensitive FE model may be compromised. In the present paper, a series of model validations are proposed that rely on the global and local response of the material during or after bending. A benchmark specimen and an air bending set-up have been developed from a numerical design of concepts and fine-tuning of tool dimensions, ensuring the appropriate bending conditions. Local validation is pursued using stereo Digital Image Correlation (DIC) to capture the strain fields, generated during plastic bending of a 12 mm thick S690QL plate. The crux of the problem is twofold: firstly, strain calculation methods used in DIC and FEA are fundamentally different, hampering a correct and honest comparison. Secondly, consistent point-to-point comparisons of experimentally acquired (DIC) and numerically computed (FEA) strains are more susceptible to uncertainties related to processing settings and differences in coordinate frame. Moreover, the main advantage of the introduced ground truth validation is the ability to level the FEA data through identical filters as the DIC experiment. Unlike a direct comparison, this levelling approach auto-adopts an unconditionally equal strain calculation, based on nodal displacement fields, independently of a local (shell) or global (solid) element formulation. This paper aims at clarifying the need for this ground truth validation in pursuance of higher fidelity FE-models for metal forming simulations.

Keywords FE validation · Stereo DIC · Numerical modelling · Cold-forming process · Air bending · HSS

Introduction

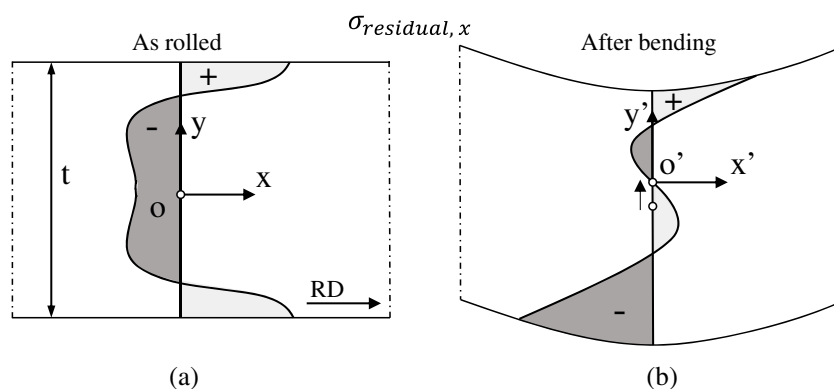
In recent years, modern industry has adopted a need for continuous innovation. Here, the importance of research is reflected in countless advances towards materials science and engineering. High Strength Steel (HSS) grades, such as S690QL, are frequently implemented for their desirable properties, such as an increased yield strength, impact toughness and fatigue resistance, allowing for thinner

members [1]. Typical applications include heavy-duty machinery, lifting equipment and civil constructions, where the emphasis lies on the overall weight and durability. For example, telescopic cranes adopt a series of hollow HSS members with square, rectangular or oval cross sections, derived from consecutive forming processes [2]. Thickness reduction rolling is widely used to manufacture flat HSS plates of specific thicknesses. From literature [3, 4] it was found that rolling leads to tensile residual stresses at the material surface and compressive residual stresses in the center of the plate, as shown in Fig. 1a. Here, a stress equilibrium must be satisfied through the thickness of the material. After rolling, detrimental effects of enlarged voids and stretched out grains are usually reduced through tempering or annealing [5]. Rolled HSS plates then rely on a secondary forming processes to attain the specific

✉ S. Gothivarekar
sanjay.gothivarekar@kuleuven.be

¹ Department of Materials Engineering, KU Leuven, Campus Ghent, Gebroeders De Smetstraat 1, 9000, Ghent, Belgium

Fig. 1 Residual stress distribution through the plate thickness in x-direction: **a** after rolling and **b** after elastic recovery of cold bending, orthogonal to the rolling direction



shape of a hollow steel members. In general, two main methods exist, continuous roll-forming and press-brake forming, where cold-bending is regarded as the dominant deformation mode of press-brake forming. Bending is often preferred to roll-forming because of a greater surface finish, level of precision and increased efficiency [6]. These benefits especially apply for moderately thick HSS, where roll-forming is less suitable. Nevertheless, several authors [7–9] have shown that care must be taken when bending rolled steel plates, as tool-dimensioning, friction and material orientation play a major role. Bending perpendicular to the rolling direction is mostly performed as it requires less bending force because the material's ductility is stretched. Furthermore, the bending radius must be sufficiently large to avoid excessive stain localisation and surface cracking. In Fig. 1b the resulting stress state is shown after a spring back step of a cold bending process, where a tensile residual stress is found near the surface of the inside of the bending root. This is mainly a result from the large compressive stress built up during bending followed by stress relaxation that reopens the bend during springback. In addition, this induces a slight shift of the neutral axis towards the inner surface, from O to O'. Conversely, the outside of the plate heavily stretched during bending followed by compression after springback [8]. Since formability is directly attributed to the material microstructure, steel manufacturing and subsequent metal forming must be carefully controlled. The latter can be done with the aid of finite element techniques. Several authors [6, 10, 11], have studied the effect of forming on the mechanical behaviour of HSS plates, by means of advanced Finite Element Analysis (FEA) and experimental test campaigns. Since cold-forming introduces a significant amount of residual stresses, shown in Fig. 1b, the local mechanical behaviour of the formed component is affected. Additionally, the average ratio of residual to yield stress has shown to be significantly different for HSS grades compared to conventional steel grades, causing the need for a better understanding of cold-formed HSS components [12].

For bent sections, the most critical area is often located on the inside of the bending root, due to large compressive

strains and surface porosities caused by the punch contact. Advanced numerical models are often developed for accurate predictions of residual stresses and strains as they are imperative for the life assessment and overall integrity of metallic structures and applications [4, 11, 13]. However, an incomplete or rudimentary validation of these models can potentially lead to precarious situations of data-corruption. Therefore, DIC is widely used as a validation tool because of its robustness and versatility. Nevertheless, for many applications a one-to-one relationship between the DIC test data and the FEA data can be lacking whatsoever, leading to a wrong comparison between the two. First and foremost, the strain calculation method adopted in DIC and FEA differ fundamentally. In addition, FE validations often suffer from uncertainties related to calibration, frame misalignment and probing errors [14]. This paper aims at clarifying the need for consistent FE validation using DIC data in metal forming applications. To this end, a large deformation cold-bending process is studied, both numerically and experimentally. A benchmark specimen, made of S690QL HSS, has been designed for FE modelling and subsequent validation using DIC. Section “Experimental” provides a detailed description of the investigated material, specimen geometry and the adopted experimental set-up and measurement techniques. Additionally, the different strain calculation procedures used in DIC and FEA are discussed. Section “FE model” introduces the FE model to simulate the bending process and subsequent springback. Finally, several validation strategies are discussed in “Model validation”, based on quantitative comparisons of the bending force, bend angle and measured strain fields. Here a distinction will be made

Table 1 Mechanical properties of S690QL [15]

S690QL	σ_y [MPa]	σ_{UTS} [Mpa]	ϵ [%]
RD	748.4 ± 1.4	804.4 ± 1.5	37.7 ± 3.6
	r_0	r_{45}	r_{90}
Lankford	0.907 ± 0.001	1.028 ± 0.015	0.894 ± 0.013

Table 2 Chemical composition of S690QL [15]

C	Mn	P	S	Si	Cr	Ni	Mo
0.2	1.7	0.02	0.01	0.8	1.5	2	0.7
N	Nb	Ti	Cu	B	Zr	V	CEV
0.015	0.06	0.05	0.5	0.005	0.15	0.2	0.77

for the global response, followed by the local response of the bending model, where the justification of a full-field method will be elaborated on.

Experimental

Material and specimen

Table 1 shows an overview of the mechanical properties of the investigated HSS plate [15]. This grade is in compliance with EN10025-6 and has an average experimental yield strength of 748.4 MPa in the rolling direction (RD). This grade has been quenched (Q) and tempered to achieve great strength and durability, and it has a specific impact toughness at lower temperatures (L). Tempering or briefly re-heating just below the critical recrystallisation temperature is performed to improve the toughness and recover formability of the otherwise hard and brittle microstructure, resulting from quenching [5]. In general, the resulting microstructural features can have a significant influence on the mechanical behavior of HSS. For example, precipitated carbide particles exhibit higher hardness and different plastic inhomogeneity thereby increasing the notch-sensitivity through microscopic stress concentrations. The chemical composition, displayed in Table 2 [15], shows the limitation of carbon content to 0.2 and indicates the fraction of the prominent alloying elements that improve the strength and corrosion resistance. Nevertheless, large deformations resulting from secondary forming processes can strongly affect the resulting mechanical behavior. To

assess this effect, a specific material modelling strategy was proposed.

Here, isotropic elasticity was modelled using a Young’s modulus $E = 209$ GPa and Poisson ratio $\nu=0.33$. Denys et al. [15] investigated the plastic anisotropy of S690QL, wherefrom Lankford ratios are shown in Table 1, indicating relatively weak plastic anisotropy. Consequently, the plastic behaviour of S690QL was modelled using the Von Mises yield criterion. The solid blue curve in Fig. 2a shows the pre-necking true stress-true plastic strain curve, acquired via a quasi-static tensile test. This data consists of the initial yield stress at 748.4 MPa, indicated by the diamond, followed by strain hardening data up to ϵ_{max} of 0.055. Hereafter, the plasticity was fitted using an inversely identified post-necking p -model [16], from the diffuse neck as described by Zhang et al. [17], using Finite Element Model Updating (FEMU) and DIC. This approach accounts for accurate strain hardening and large plastic strains expected to be in the order of $\epsilon_{pl}=0.3$ for this bending process. The p -model, represented by the solid black curve in Fig. 2a, can be described by:

$$\sigma_{eq} = \begin{cases} K(\epsilon_{pl}^{eq} + \epsilon_0)^n & \text{if } \epsilon_{pl}^{eq} \leq \epsilon_{max} \\ K(\epsilon_0 + \epsilon_{unif})^n + Q \left[1 - e^{-p(\epsilon_{pl}^{eq} - \epsilon_{unif})} \right] & \text{if } \epsilon_{pl}^{eq} > \epsilon_{max} \end{cases} \quad (1)$$

The parameters for this model can be found in Table 3. Once the maximum uniform strain ϵ_{max} is exceeded, the true stress σ_{eq} gradually increases before saturating around 940 MPa. This stress plateau is mainly attributed to the relatively high p -value. A lower p -value e.g. $p - 1\sigma$, with σ the standard deviation associated with the identification procedure, would lead to stronger work hardening. This is plotted as the solid red curve in Fig. 2a. Conversely, less work hardening was modelled by the higher p -value of $p + 1\sigma$, plotted as the dotted red curve. The effect of deviating strain hardening behaviour is considered important and was therefore included in the current study.

Fig. 2 a Pre –and post-necking strain hardening behavior of S690QL 12 mm along the rolling direction, b Bending sample with geometry set and corresponding experimental DIC set

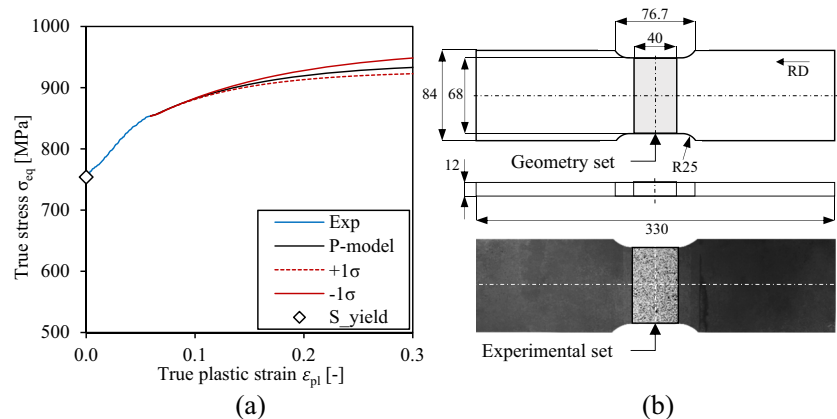


Table 3 Inversely calibrated parameters of p -model [17]

K [MPa]	n	ε_0	ε_{max}	p	Q
1016.4 ± 2.7	0.0624 ± 0.0027	$9e-6 \pm 0.1e-6$	0.055	10.16 ± 1.94	94.69

Air bending set-up

Heavy-duty machinery frequently employs HSS members in long and slender configurations [11]. Therefore, rolled plates are cut into a specific shape and consequently formed at room temperature, to the desired outline. To reproduce the resulting stress state of these members, bending samples have been designed with a specimen width-to-thickness ratio w_s/t of at least 5. Thereby avoiding excessive plasticity or multiaxial stresses found near the edges [7]. The resulting benchmark specimen, shown in Fig. 2b has a central width of w_s of 68 mm and thickness t of 12 mm. The bending process is performed perpendicular to the rolling direction. In addition, the dimensions of the air bending set-up, shown in Fig. 3a, were carefully chosen. This resulted in a bending ratio $\rho = r_p/t$ (punch radius to thickness) of 2 and die-width to thickness ratio w_d/t of 10 [9]. The samples were removed from a rolled plate, by water jet cutting, followed by the bending operation, that takes place in the lower testing area of a (Zwick Roell Z250) tensile test machine, shown in Fig. 3b. The absolute cross-head displacement δ_{Punch} was carefully measured and corrected using a stereo DIC set-up, ensuring an equal travel distance with the model. Therefore, a set of markers, was applied to the rigid tools and tracked using a data extraction.

DIC method

It is clear that DIC is prevalent in experimental mechanics literature and can offer an added value for deriving higher fidelity FE models [14, 17]. Since bending causes in-

and out-of-plane deformation, a stereo DIC set-up was used to measure the residual strains at the bottom surface of the bent sample. An approach is introduced here, that quantifies these strains at several distinct bending steps. Commercial DIC code MatchID 2019 was adopted for capturing and processing images [18]. Allied Vision Manta G609 CCD sensors were used, with lenses of focal length of 25 mm. Here, a relatively large stereo angle, specified in Table 4, was chosen to acquire an acceptable out-of-plane accuracy. For the application of the speckle pattern, the sample is sandblasted, degreased and taped first. Figure 2b demonstrates how carefully taping the specimen can ensure a correctly dimensioned experimental set. Subsequently, a base coating of white spray paint is applied, followed by a fine mist of black spray paint. The current workflow was fine-tuned in previous studies and tends to deliver a consistent speckle pattern quality with an average speckle size of 4.4 ± 0.1 pixels. To ensure a good correlation for this large deformation process, images were captured at four consecutive bending steps with a fixed, incremental travel distance of 10.2 mm. This resulted in a total punch displacement of $\delta_{Punch} = 40.8$ mm, approximately corresponding to a 90° angle. After every bending step the sample is removed from the air-die and placed in the DIC set-up, for image capturing.

In total five images are taken, containing two reference and four deformed configurations that are uploaded to the MatchID Stereo-module.

For post-processing, the optimum DIC parameters were determined through a performance analysis, shown in Fig. 4. In this graph the maximum strain is plotted against the strain

Fig. 3 Air bending of high strength steel: **a** schematic overview, **b** practical set-up

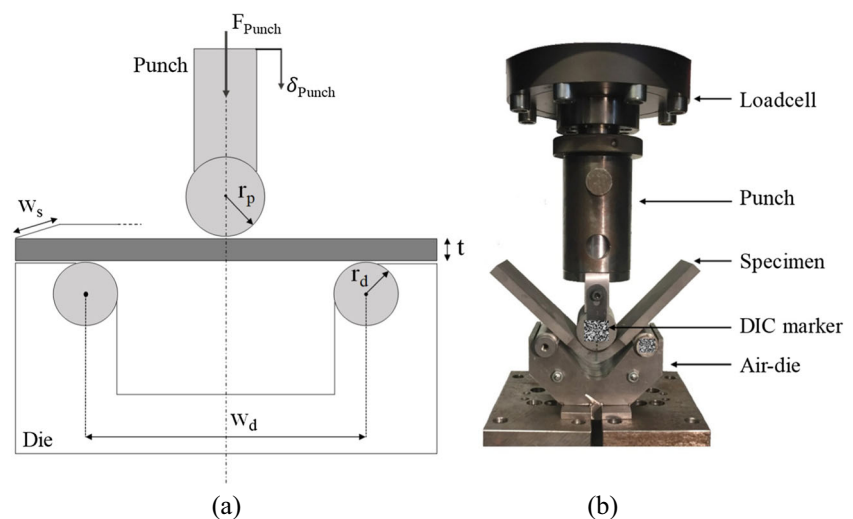


Table 4 Experimental and processing parameters of DIC method

Experimental parameters	Value	Processing parameters	Specification/Value
$\theta(x)$ [°]	0.61	Matching criteria	ZNSSD
$\phi(y)$ [°]	20.57	Shape function	Affine
$\psi(z)$ [°]	0.005	Interpolation function	Bicubic splines
Tx [mm]	−124.5	Progress history	Spatial
Ty [mm]	−3.291	Subset size (SS) [px]	29
Tz [mm]	11.98	Step size (ST) [px]	8
Noise level [%]	0.3468	Strain Window (SW)	19
Camera resolution [HxV]	[275×2206]	Strain tensor – Polynomial	Euler-Almansi-Q8
Strain resolution [$\mu\text{m}/\text{m}$]	50	Virtual Strain Gauge (VSG) [px]	137

resolution for several correlations with subsets sizes varying from 21 to 35 pixels, step sizes (ST) 6 to 12 pixels, affine and quadratic shape functions, Q4 and Q8 interpolation functions and strain window (SW) sizes 11 to 21. The obtained results show a similar trend from left to right, where the strain resolution increases with smaller virtual strain gauge size ($VSG=(SW-1)\times ST$). Further, large VSG’s combined with lower order polynomials are less suitable for describing complex heterogeneous deformations, whereas relatively small VSG’s cause a reintroduction of noise, as shown in a previous study [14]. This research showed that the inverse proportional relation of accuracy and precision to the strain-window size was more pronounced for regions governed by heterogeneous deformation.

From Fig. 4, it can be concluded that a quadratic shape function has little added value, given the large bending radius. Nevertheless, the performance analysis helps to select optimal DIC settings by assessing the trade-off between strain resolution and signal reconstruction (e.g. maximum principal strain). This reasoning should minimise the resolution of the measurement whilst reproducing maximum signal convergence. An optimisation of this cost function is represented by point A of Fig. 4. This optimum was derived with a subset of 29 pixels, step size of 8 pixels

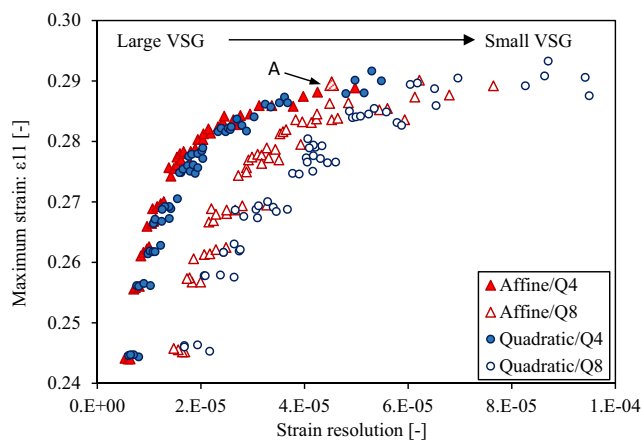


Fig. 4 Performance analysis of bending process for $\delta P_{punch,max}$

and strain window of 19 with an affine shape function and Q4 interpolant. Further details of the experimental and processing parameters are stated in Table 4. The obtained strain fields now serve as a reference for the experimental data that can be used to validate the FE model, as described in “Local response: Direct FEA vs DIC” and “Local response: Levelled FEA vs DIC”. However, the fundamental differences between strain calculation methods in FEA and DIC are considered first in the following Section.

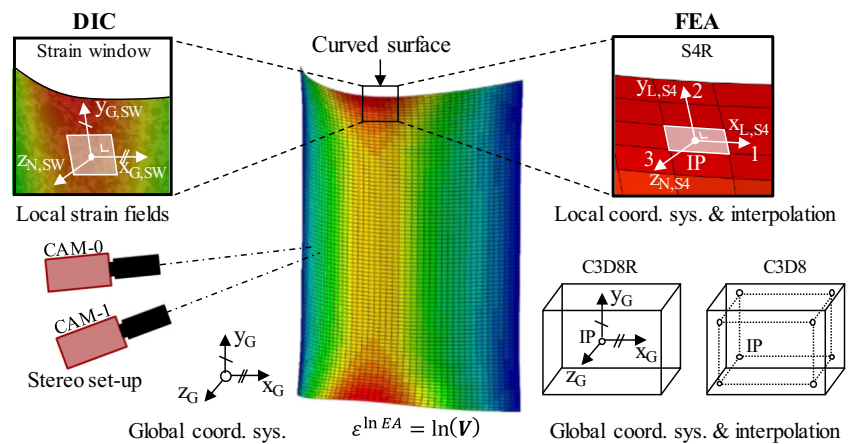
DIC and FEA conventions

To justify the need for a well-grounded validation method, a few important, underlying principles of DIC and FEA will be discussed as well as the fundamental differences in the strain calculation procedure. When modelling metal forming of thick plates (thickness larger than 8 mm), 3D solid elements are required to probe results through the specimen thickness [19]. Generally, important numerical outputs such as, principal strains at the free surface, are often compared with experimental measurements, by means of validating the FE model. However, due to intrinsic differences in the strain calculation procedure and associated vector conventions, a direct comparison is usually discouraged [14].

- DIC reference system and strains:

In this study, subset-based DIC is adopted, that compares relative grey values of a unique speckle pattern between consecutive images. In detail, changes in shape and position of a subset, with size $N\times N$ pixels, are tracked in several images of an experiment. Subsequently, strains are calculated in a local varying coordinate frame based on the deformation gradient \mathbf{F} [20]. Here, the initial topology of the specimen is measured relative to a global coordinate system, determined by a best plane fit. A local planar area is then defined by the strain window, shown in Fig. 5. Further, surface orientations are fixed by a normal vector, $\mathbf{Z}_{N,SW}$ and two tangent vectors, $\mathbf{Y}_{G,SW}$ and $\mathbf{X}_{G,SW}$, that are in the plane of the strain window and aligned with the global coordinate system. Inexorably, these directions are determined by the

Fig. 5 Deformed shell part, tied to the bottom of specimen with strain derivations found for DIC and FEA



surface normal that can change in shape and orientation, as deformed tensor conventions are adopted. The strain calculation is based on a logarithmic Euler-Almansi strain tensor $\varepsilon^{\ln EA}$, that computes a local deformation gradient \mathbf{F} , as described by Eq. 2. With \mathbf{V} the stretch tensor derived through the cauchy theorem of polar decomposition [14]. From the conventions stated above, it can be concluded that MatchID expresses strain fields according to a local varying coordinate system.

$$\varepsilon^{\ln EA} = \ln(\mathbf{V}) = \ln(\sqrt{\mathbf{F}\mathbf{F}^T}) \quad (2)$$

– FEA reference system and strains:

Conventional, quadrilateral S4(-R) shell elements typically adopt a local co-rotational coordinate system and interpolation scheme. This accounts for rigid body rotation of the material, allowing for a better interpretation of curved edges [21]. Stresses and strains in a shell part are defined by means of local directions in space. First, a default local direction: **1**, is projected from the global x -axis to the surface, denoted as $\mathbf{X}_{L,S4}$ in Fig. 5. Secondly, the right-handed system is completed through the second direction: **2**, corresponding to $\mathbf{Y}_{L,S4}$ and a positive surface normal $\mathbf{Z}_{N,S4}$. Typically, finite-membrane-strain elements express the stresses and strains relative to the material directions in the current configuration. By default, FE software outputs the logarithmic strains (LE) or ε^L as:

$$\varepsilon^L = \ln(\mathbf{V}) = \sum_{i=1}^3 \lambda_i \mathbf{n}_i \mathbf{n}_i^T \quad (3)$$

Here, λ_i and \mathbf{n}_i represent the stretches and directions for the current configuration, respectively [19]. The FE-user can then request strain values from the integration points (IP), located in the centre of the element in case of reduced integration. For shell elements these are expressed according to two local directions (**1**, **2**) and one normal direction (**3**), as shown in Fig. 5. Additionally, nodal strains, are obtained through an interpolation from the integration

points to the nodes, using element shape functions. When looking to probe nearer to the surface, solid elements can benefit from full integration as it introduces more calculation points in the elements. In that case, the locations of the IP's are based on a Gaussian quadrature rule, implying a weighted sum of function values at specific points in the element [22]. However, fully integrated elements often exhibit overly stiff behaviour for bending simulations and plastic deformation in general. For example, C3D8 Solid elements with $2 \times 2 \times 2$ integration points, can provoke shear locking problems [22]. Therefore, reduced integration is often resorted to, e.g. C3D8R element with hourglass controls, as it also decreases the overall computation time.

It is clear that the assessment of surface strains implies a consideration of the discrepancies found between the calculated integration point values and interpolated nodal values. To overcome this possible probing error, a shell part can be tied to the solid specimen in the area of interest. As a result, the distance between the calculation points and probed node sets can be minimised and the surface strains are expressed according to a local co-rotational coordinate system. This improves the correspondence with conventions found for DIC provided that i) there is no rigid body material rotation and ii) the surface normal does not change direction during the experiment. It is clear that the aforementioned differences in strain conventions are expected to influence the direct comparison, discussed in “[Local response: Direct FEA vs DIC](#)”. Contrarily, the method introduced in “[Local response: Levelled FEA vs DIC](#)” processes the FE data through the DIC calculation procedure, resulting in a ground-truth comparison.

FE model

In the current paper, ABAQUS/Standard 2019, was employed to calculate the stress-strain state of a high strength steel plate after bending. The modelled bending

process considers non-linear strain hardening during bending followed by elastic springback. The model consists of a 3D deformable solid specimen and two discrete rigid parts. In Fig. 6, the assembly is shown, as well as contact properties, boundary conditions and elements used. Note that the z-axis is pointed downwards, corresponding with global orientations found in MatchID. Surface-to-surface contact is adopted for the punch and die rollers. During bending experiments, high pressure lubrication oil was used, corresponding to a friction coefficient of $\mu=0.05$ [23]. Despite the symmetrical nature of the assembly and process, the full geometry was modelled, simplifying the data-extraction used for comparative analyses with experimental data. A mesh convergence study resulted in a total of 194400, 8-node linear brick elements with reduced integration and hourglass controls. As mentioned before, a shell part with infinitesimally small thickness of $1\ \mu\text{m}$, was tied to the bottom of the specimen to investigate the influence of different element types. Further, mesh refinements were introduced in the contact areas and near the centre of the specimen. The bending process is solved in two steps, a general non-linear, quasi-static step, followed by a dynamic, implicit step. In the first step, a vertical displacement, corresponding with the experiment, is applied to the rigid punch. Hereafter, large tensile and compressive stresses are found near the outer and inner fibres respectively. This unbalanced stress distribution counteracts the large bending moment that deformed the cross-section [24]. In the next step, the punch returns upwards and loses contact, allowing the specimen to springback, to its final bend angle. This form of elastic recovery reassures a balanced stress equilibrium through the plate thickness, as previously shown in Fig. 1b. Since this phenomenon occurs instantaneous it is considered in a dynamic step, taking account for mass and acceleration effects, significantly improving the models convergence. The numerical approach provides valuable information at the inside of the bending root, where DIC measurements are hindered due to contact the punch [25]. In correspondence with the incremental approach of the experiment, the

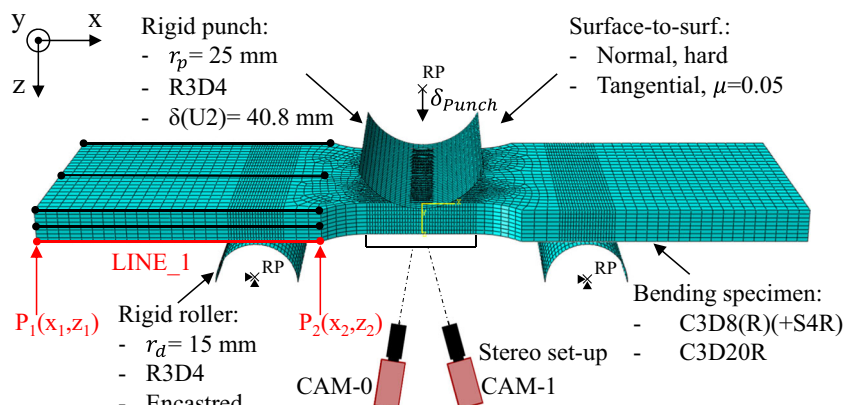
model is solved for four consecutive bending steps to a maximum punch displacement of 40.8 mm. In the following Sections, several validation methods are introduced, ensuring the validity of the numerical model. First the global responses are evaluated such as, the force-displacement curve, followed by bend angle and springback. For this analysis a maximum continuous bending step is adopted for the experiment and simulation as opposed to the incremental approach defined in “DIC method”. Second, the residual strain fields derived from the model will be compared with surface strains by means of a line-extraction method, elaborated in “Local response: Direct FEA vs DIC”. Ultimately, a full-field validation method is discussed, in “Local response: Levelled FEA vs DIC”, that quantitatively compares a specific set of the model with the experimental results, using identical processing filters.

Model validation

Global response: Bending force

To ensure the validity of the FE model, multiple standard outputs will be validated initially accompanied by the newly developed validation method that is capable of analysing several parameters at once. First, the force-displacement response is analysed to indicate any incipient differences between the FE model and experiments, shown in Fig. 7. Since a relatively small deviation was found for experimental data, only two bending tests are plotted and compared here for the complete travel distance of $\delta P_{punch}=40.8\ \text{mm}$. The FEM data consists of three curves derived using different element formulations. When comparing with the experiments, it is clear that linear brick elements display a good correspondence for both reduced (C3D8R) and full integration (C3D8), whereas quadratic elements (C3D20R) result in a larger maximum force. In general the FE data have a slightly steeper slope and therefore an incrementally larger stiffness than the experiment. This is mainly

Fig. 6 Assembly of 3D-model with modelling input parameters and schematic representation of 3D stereo DIC set-up



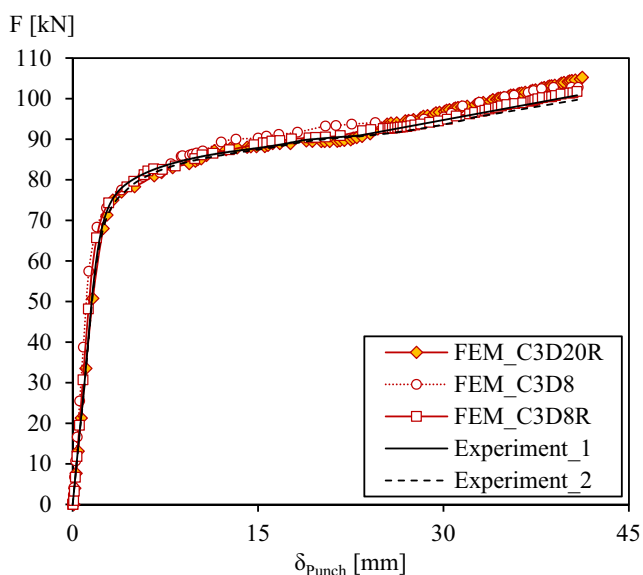


Fig. 7 Comparison of the bending force as a function of the punch stroke for different element types

attributed to the rigid behaviour of the punch and rollers compared to a lower stiffness of the set-up and testing frame. To account for the artificial displacement induced by the cross-head, a DIC displacement measurement was performed, by means of markers, shown in Fig. 3b. As a result, an average deformation of the set-up was noticed of approximately 1.46 mm for a displacement of 10.2 mm. This correction was imposed, by calculating the frame stiffness and correcting the total displacement. At a larger travel distance, the two curves coincide, leading to a good correspondence. Here, a maximum bending force amounts to 99.78 kN and 99.42 kN for experiment 1 and 2, respectively. The FE model, delivered values of 100.71 kN, 101.75 kN and 104.81 kN for C3D8R, C3D8 and C3D20R element types respectively. Again this confirms a good resemblance. Although this analysis results in a first indication that the model is valid, it neglects other important outputs, such as the resulting geometry or strain distribution.

Global response: Bend angle

In this Section, the initial θ_i , final θ_f and springback angles $\Delta\theta$ are evaluated. The difference in initial and final angle, called springback, is caused by the recovery of elastic deformation while the bending load is removed [9]. At the maximum punch displacement, substantial tensile stresses accumulate near the outside of the bend, comparable to a stretched spring. Conversely, on the inside, compressive stresses resemble a compressed spring. Once the load is removed, the specimen releases a significant amount of potential elastic energy, counteracting the deformation imposed by the bending process [24]. Consequently, the

final bend angle is obtained. The experimental results, plotted in Fig. 8a, include angle measurements at maximum displacement and after springback using an angle ruler with an accuracy of $\pm 1'$. From literature [9], an analytical approximation for springback can be expressed by:

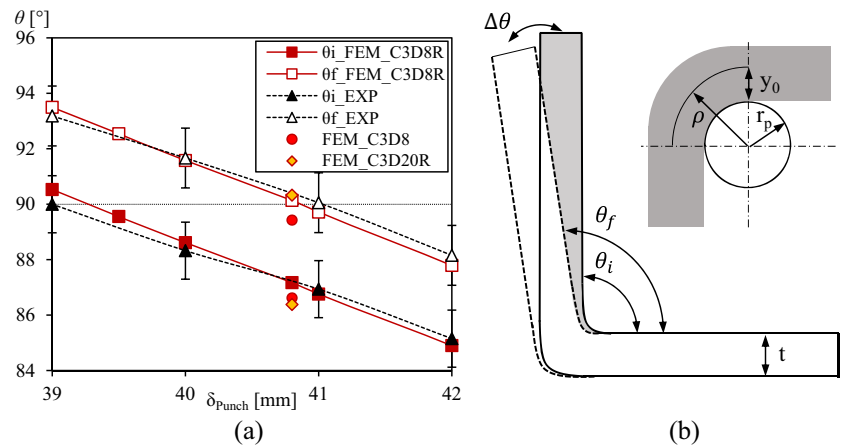
$$\Delta\theta \approx \frac{-3\rho S}{E't} \quad (4)$$

This equation relies on the internal stress $S(= 2/\sqrt{3}\sigma_y)$, plane strain modulus $E'(= E/(1 - \nu^2))$, plate thickness t , target bend angle θ , and the bend radius $\rho(\approx r_p + y_0)$ as seen in Fig. 8b. Here the bend radius is approximated by the summation of the punch radius $r_p(=25 \text{ mm})$ and the distance to the neutral axis $y_0(=5.5 \text{ mm})$ derived from the FE model. To attain the bend angles from the FE model, a script was developed that extracts deformed coordinates from specific points in the model. Several node sets are constructed, each representing two nodes along the length of the solid part, shown in Fig. 6. This resulted in angle values through the thickness of the specimen. For example, Line-1 consists of two points, P1 and P2, with original coordinates (x,z) , located in areas with little to no deformation. The difference in coordinate values of these two points are then extracted at the maximum displacement and after springback, wherefrom the bend angles can be calculated. The results of these numerical bend and spring back angles as a function of the punch displacement are plotted in Fig. 8a. Similarly to the force analysis from previous section, the results of two other element types are plotted for the punch displacement of 40.8 mm. This shows that full integration delivers a slightly smaller spring back, whereas quadratic elements yield larger springback. Also here C3D8R elements seem to be more appropriate. The experimental angles represent the average value of two bending tests with equal maximum displacements. At smaller displacements, it can be noticed that the modelled bend angle slightly overestimates the actual value of both initial and final angle, potentially attributed to an incrementally larger modelled stiffness. However, the overall slope of numerically and experimentally derived angles shows an acceptable resemblance. Average spring back values of 2.945° and 3.162° can be found for the simulation and experiment, respectively. For the mechanical properties stated in Table 1 of “Experimental”, and a bend angle $\theta=90^\circ$, Eq. 4 yields a analytical value of $\Delta\theta \approx 2.543^\circ$, comparable with the model and experiment.

Local response: Direct FEA vs DIC

Another method, pertinent for evaluating this bending model is the comparison of a data extraction along the bottom surface. In the MatchID results module, an

Fig. 8 **a** Comparison of bend angle as a function of the punch displacement. **b** Overview of the bending parameters

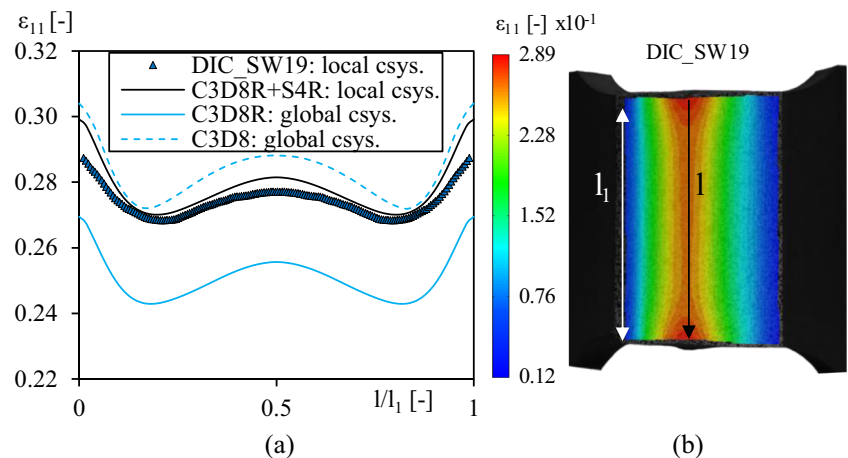


extraction of the principal strains can easily be performed for a specified line segment that snaps to the calculated data-points in the area of interest (AOI) [25]. In Fig. 9a, the results of the maximum principal strain as a function of the normalized width l/l_1 are displayed, for the DIC data and FE data obtained with different element types. Fig. 9b shows the experimental DIC data with the specific, demarcated AOI where a line-extraction is performed near the centre of the specimen. The FE-data represents the probed nodal values, along the middle of bent area at the bottom side. For this study, three different element types were investigated, solid elements in reduced integration (C3D8R), full integration (C3D8) and shell elements with reduced integration (S4R) of a tied shell part. A negligible effect of fully integrated shell (S4) elements was noticed and therefore not considered. It can be stated that the deformation of this slave shell part is entirely defined by the master solid body in the tie constraint [22]. The fundamental issue here occurs when directly comparing the surface strains as this does not consider the differences in conventions of DIC and FEA, as described in “DIC and FEA conventions”. In areas of highly localised deformation and rigid body rotation, solid elements can deliver ambiguous

results as the global coordinate reference and interpolation is known to be more sensitive to the elements orientation in global space [21]. This can be resolved through the use of local coordinate interpolation functions adopted by iso- or subparametric elements, e.g. S4R-elements as shown in Fig. 5 [21]. This explains why the results obtained from C3D8R elements, represented by the solid blue curve, initially discard the validity of the model as opposed to the results obtained from the tied shell part (i.e. C3D8R+S4R). This shell-derived data displays the best resemblance with experimental data, having an RMSE value of 0.005.

In addition, for solid elements, full integration (C3D8) delivers better results. However, the same fundamental mistakes are made by directly comparing data obtained using different conventions. These complications feed into the uncertainty of adopting solid elements as a valid reference for the FE model, especially for the locally deformed areas near the centre and at the ends of the specimen. Here, a minimum RMSE value of 0.012 was found for C3D8. Contrarily, shell elements more accurately reproduce these pronounced deformations through a local coordinate system along with the computation and interpolation of strain values nearer to the material surface. In Fig. 10, several other data-sets

Fig. 9 **a** Line-extraction of the maximum principal strain: ϵ_{11} , for a bend angle of 90° . **b** DIC data along bottom side, obtained with a strain window of 19



were added, to indicate the effect when adopting different modelling and DIC settings. For instance, a higher frictional coefficient of 0.15 resulted in lower values of residual strain near the lower bound. Generally, higher friction brings about an increased force demand and stick-slip problems in contact areas [8]. As mentioned before in “Material and specimen”, the effect of strain hardening was also investigated here. The strain hardening parameter p , used to describe the hardening law via Eq. 1, has a nominal value of 10.16 with a standard deviation of $\sigma = \pm 1.94$. The effect of this deviation on the predicted strain distribution can also be described by means of these boundaries. Here, a higher p -value of $p + I\sigma$, displayed as the dotted black curve in Fig. 2a, results in less work hardening, ultimately leading to higher residual strains, shown as the upper bound or dotted red curve in Fig. 10. Further the effect of different strain windows can be visualised. It is clear, that a relatively small strain window of 11 results in a noisy distribution, whereas the large strain window displays an underestimation due to excessive smoothing. Although the PA-analysis pointed towards an ideal SW of 19, a smaller SW is more likely to have a better signal reconstruction. This further illustrates how user-defined settings can influence certain validation methods, such as this line-extraction. In addition, the use of solid elements can be discouraged for direct comparison of the local response. Adversely, a shell-tie approach was adopted to derive a more grounded comparison along the extraction. This method narrowed the gap with DIC conventions, leading to a reliable validation of the maximum principal strain distribution. Besides the potential error with respect to the adopted material model, several slight deviations can be attributed to differences in probing region or measurement errors. To mitigate these uncertainties, a

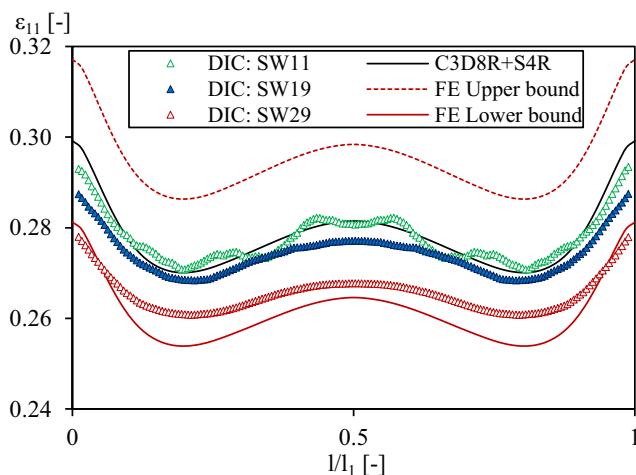


Fig. 10 Sensitivity of the line-extraction of principal strain: ε_{11} , for three experimental strain windows: SW11, -19 and -29 and for different strain hardening data or friction values of the FE model

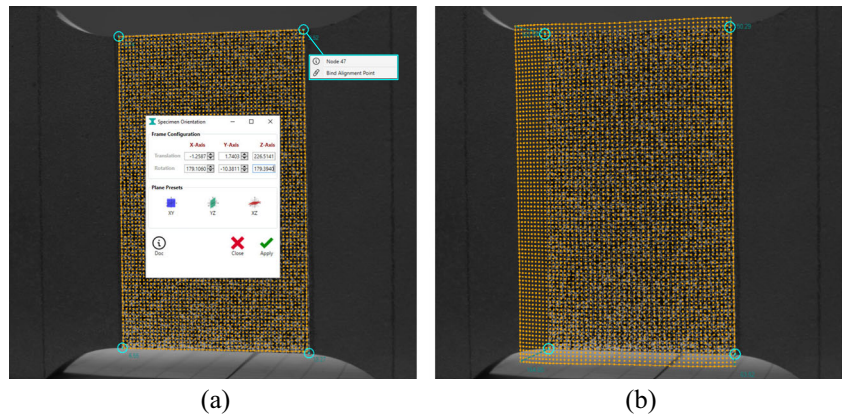
full-field validation procedure is presented and evaluated in the next Section.

Local response: Levelled FEA vs DIC

The aforementioned validation criteria have shown different methods to verify the accuracy of the bending simulation. Initially, reliable experimental data, derived from a specific measuring technique and testing method, should act as a reference for the true behaviour of the specimen. In the current study, a stereo DIC set-up was chosen to measure the strain fields at the material surface, with relatively high precision. Direct comparisons between FE and DIC, by means of a data-extraction, has been discussed in the previous Section. The last method, introduced here, is focussed on a full-field comparison that considers the differences between FEA and DIC, explained in “DIC and FEA conventions”. MatchID provides the opportunity of an experimental validation by processing FEA data through identical processing parameters and filters (subset, step, strain window, shape function, interpolation and so on) [18]. These settings are specific to the actual DIC experiment and can be found in Table 4 of “DIC method”. The goal is to level FEA data, allowing for a truthful comparison [26]. The workflow outlined here relies on two built-in modules: FEDEF and FEVAL. The FEDEF-module generates a set of synthetic images that consider the deformation obtained from the model [14]. First, a surface set is created that corresponds with a specific geometry of the test sample, in this case the bottom surface shown in Fig. 2b. Here, the nodal information and element connectivity of the set are converted to an initial .mesh file. This mesh is then oriented and aligned on top of the speckled area of interest (AOI) of the reference image through a coarse specimen orientation, based on translating and rotating the set, followed by a fine orientation where alignment points are bound to the speckle pattern. This establishes the connection between the geometry and experimental set or AOI, as seen in Fig. 11a.

Additional experimental data is considered by uploading the camera calibration parameters and introducing the measured noise level of 0.347%, as found in Table 4. Secondly, the deformed nodal coordinates are extracted from specific frames and visualised, as shown in Fig. 11b. Finally, a new set of images is created by deforming the reference image according to the nodal displacements. The FEVAL-module then performs a stereo correlation of the numerically deformed images using the original DIC experiment and settings as a reference. Hereafter, the maximum principal strains can be visualized as colour plots, illustrated in Fig. 12. Here, the results are plotted for the original DIC experiment and virtual DIC experiment, generated by the FEVAL-module and based on

Fig. 11 FEDEF-module functionalities: **a** Coarse and fine orientation of the mesh. **b** Visualisation of the deformed mesh



the numerical deformation of C3D8 elements. In addition, a differences plot is generated, based on:

$$\Delta\varepsilon = \frac{\Delta\varepsilon_{DIC-FEVAL}}{\Delta\varepsilon_{DIC}} [\%] \tag{5}$$

Furthermore, Fig. 12 illustrates the levelling effect of the FEVAL-module, that resulted in little to no variation of $\Delta\varepsilon$ for different SW sizes. An increased fidelity over other validation methods can be confirmed as this approach largely neutralizes the user-paradox. As discussed in “DIC method”, the choice of SW is based on a trade-off between accuracy and precision. In this case, the performance analysis provided an optimum for a SW of 19. The maximum principal strain ε_{11} , plotted in Fig. 12, displays a relatively uniform

distribution along the width of the specimen and slightly increasing values towards the ends. The larger VSG of 237 shows a slightly smoother field compared to the smaller VSG of 109 that is generally more susceptible to noise.

This validation procedure is then continued for the maximum displacement step, as shown in Fig. 13. Here, maximum values of $\varepsilon_{11}=0.107$ and $\varepsilon_{11}=0.289$ were found $\delta P_{punch,min.}$ and $\delta P_{punch,max.}$, respectively. The final strain distribution indicates a strong difference in strain localisation near the centre of the specimen. Concurrently, the differences plots show maximum values of 6–12% in this central area, quantitatively and visually expressing potential differences in strain hardening or localisation between the model and the experiment. In this regard, the full-field

Fig. 12 Influence of strain window settings on full-field validation, for $\delta P_{punch,min.}$ and fixed subset size of 29 pixels and step size of 8 pixels

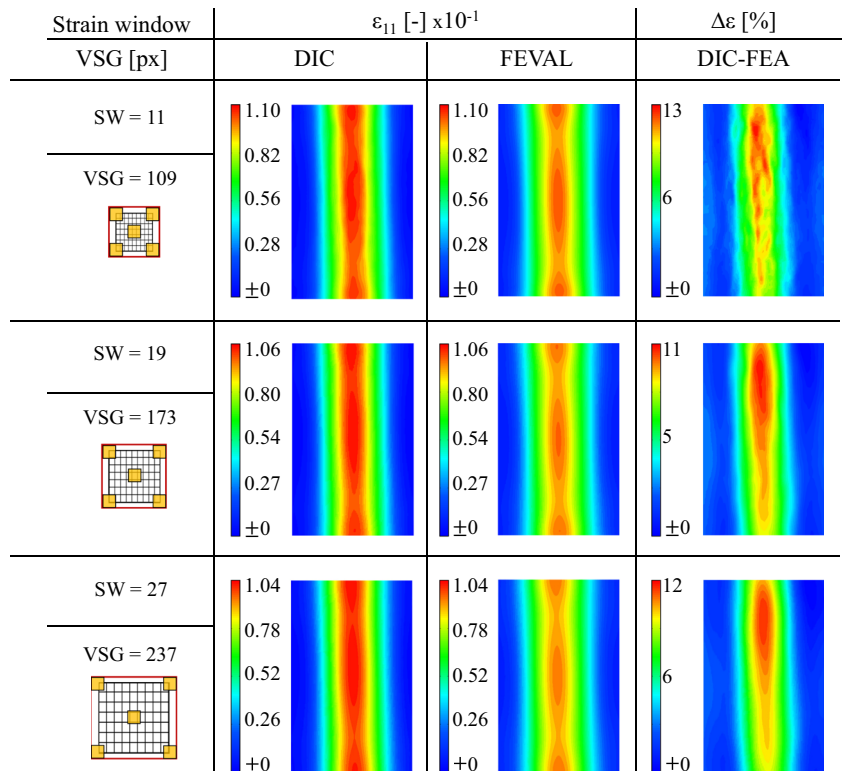
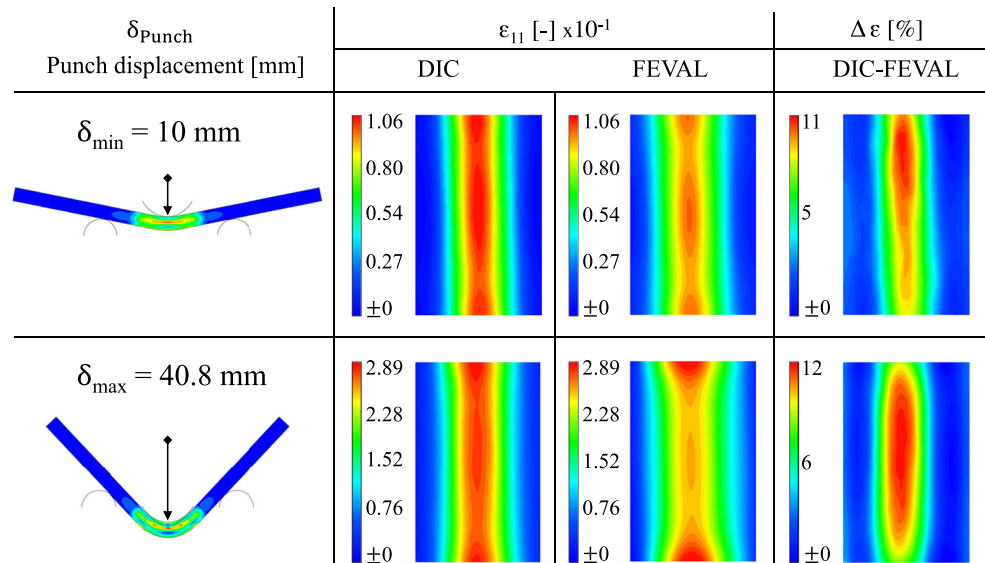


Fig. 13 Full-field validation results of the maximum principal strain: ε_{11} , obtained with C3D8 elements, for $\delta_{Punch,min}$ and $\delta_{Punch,max}$



approach provides an opportunity to identify and evaluate the true material behaviour.

As mentioned before, different element types and formulations can influence the resulting output and comparison, due to a difference in the adopted coordinate system. This effect was also investigated for the FEVAL-module, shown in Fig. 14, where a line-extraction was performed on the FEVAL data, derived with solid elements in reduced (C3D8R) and full integration (C3D8). This was then compared with the experiment and direct extraction from the shell part in the FE model. For both data-sets in the given mesh discretisation, a relatively good correspondance was found with RMSE-values of 0.006 and 0.01 for C3D8 and C3D8R elements, respectively. Here, the exclusive use of solid elements has proven to be favorable for validating the model, when the same filters and processing procedure are

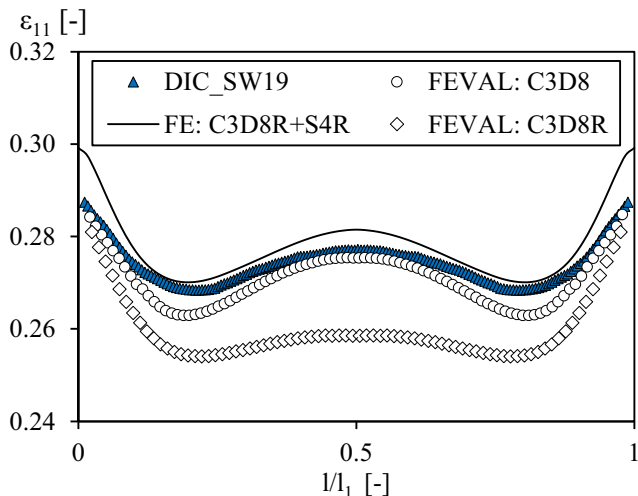


Fig. 14 Line-extraction of the maximum principal strain: ε_{11} of DIC, FEVAL and FE results, for $\delta_{Punch,max}$

applied. If this is not the case, a shell-tie approach can be used to overcome the differences in coordinate system and offset between integration point and surface points provided that i) normal vector does not change significantly and ii) rigid body rotation can be neglected. In fact, only this full-field method delivers a ground-truth comparison of the solid model and the DIC experiment. Another advantage of this method is the capability to investigate differences found for the contours in the strain fields. These vary more for the model than the experimental data, characterised by a rather uniform distribution. The largest deviations can be found near the central area and edges of the specimen, clearly indicating the room for improvement of the model. Further investigation towards the sensitivity of FEA and DIC settings could possibly provide more insight here. For example, slight deviations of the orientation, size and location of the experimental set can affect the validation. Furthermore, it is assumed that the user has adopted the appropriate correlation algorithms and processing parameters, resulting from a performance analysis, as discussed in “DIC method”.

In conclusion, this methods yields a consistent and holistic comparison between DIC and FEA. It was shown that a ground-truth comparison can play a pertinent role for the validation of metal forming simulations like air bending. Even for the maximum punch displacement of 40.8 mm, the procedure can be performed, contributing to its uniqueness when looking for full-field validation methods of large deformation processes.

Conclusion

Industrial applications increasingly rely on numerical models as well as validation methods to ensure qualitative

analyses. However, inappropriate validation methods can increase the uncertainty of the numerical results. To resolve this issue, a series of validation methods have been introduced here for a popular metal forming process of high strength steel. It was shown that an in-depth validation clarifies the major as well as minor shortcomings of the model and their relation to the inputs variables, such as strain hardening, friction and element type. The validating methods were based on different criteria, where a distinction is made between a global and local response. In the former, force-displacement and bend angle predictions are compared, where the use of finely meshed C3D8(-R) linear brick elements was justified. For the local response, a line-extraction and full-field method was performed. Firstly, a direct comparison was made between data extracted from both DIC and FEA. Additionally the effects of element type, integration, friction and hardening were studied. Secondly, a levelled comparison is made using the FEDEF-, FEVAL-procedure of MatchID. It was shown that a direct comparison is not straightforward, primarily because of the different strain calculation procedures adopted by DIC and solid elements in FEA, as well as the differences in coordinate systems and interpolation functions employed for calculating and expressing the strains. A clarifying overview of these fundamental differences and the complexity of the DIC measurement chain was introduced. From this study, it can be highly recommended to adopt a ground-truth, full-field comparison, that implies the processing of FEA data through identical filters as the experimental DIC data. This approach improves the confidence in experimental validation by means of a levelled comparison, scrutinizing the predictive accuracy of an FE model.

Acknowledgements The authors would like to acknowledge MatchID for the use of software and processing guidelines.

Compliance with Ethical Standards

Conflict of interests The authors declare that they have no conflict of interest.

References

- Li TJ, Li GQ, Chan SL (2016) Behaviour of Q690 high-strength steel columns: Part 1: experimental investigation. *J Constr Steel Res* 123:18
- Pedersen HC, Andersen OT, Nielsen TO, Dyn J (2015) *Sys Meas Contr* 137
- Cho Y, Ye H, Hwang S (2013) A new model for the prediction of evolution of the residual stresses in tension levelling. *Iron Steel Inst Japan* 53:1436
- Moen CD, Igusa T, Schafer BW (2008) Prediction of residual stresses and strains in cold-formed steel members. *J Thin-Walled Struct* 46:1274
- Fujibayashi A, Omata K (2015) Development of thermo-mechanical control process (tmcp) and high performance steel in jfe steel
- Zhu JH, Young B (2012) Design of cold-formed steel oval hollow section columns. *J Constr Steel Res* 71:26
- Soyarslan C, Gharbi MM, Tekkaya AE (2012) A combined experimental-numerical investigation of ductile fracture in bending of a class of ferritic-martensitic steel. *Int J Sol Struct* 49:1608
- Vorkov V, Aerens R, Vandepitte D, Dufloy J (2017) Experimental investigation of large radius air bending. *Int J Adv Manuf Tech* 20:42
- Weng CC, White RN (1990) Cold-bending of thick high strength steels plates. *J Struct Eng* 116:40
- Talemi RH, Waele WD, Chhith S (2017) Experimental and numerical study on effect of forming process on low-cycle fatigue behaviour of high-strength steel. *Fatigue Fract Engng Mater Struct* 00:1
- Somodi B, Kövesdi B (2017) Residual stress measurements on cold-formed HSS hollow section columns. *J Constr Steel Res* 128:706
- Shi G, Jiang X, Zhou W, Zhang Y, Chan TM (2017) Experimental study on column buckling of 420 MPa high strength steel welded circular tubes. *J Constr Steel Res* 100:71
- Ma JL, Chan TM, Young B (2015) Material properties and residual stresses of cold-formed high strength steel hollow sections. *J Constr Steel Res* 109:152
- Lava P, Cooreman S, Coppieters S, De Strycker M, Debruyne D (2009) Assessment of measuring errors in DIC using deformation fields generated by plastic FEA. *Optics and Lasers in Eng* 47:747
- Denys K (2017) PhD Thesis: Investigation into the plastic material behaviour of thick HSS using multi DIC and FEMU. KULEUVEN
- Coppieters S, Cooreman S, Debruyne D, Kuwabara T (2014) Identification of post-necking hardening phenomena in ductile sheet metal. *AIP Conf. Proc*
- Zhang H, Coppieters S, Jimenez-pena C, Debruyne D (2019) Inverse identification of the post-necking work hardening behaviour of thick HSS through full-field strain measurements during diffuse necking. *J Mech Mat* 129:361
- MatchID (2019) MatchID Modules
- Simulia (2017) Abaqus Documentation
- Wang B, Pan B (2016) Subset-based local vs. finite element-based global digital image correlation: a comparison study. *J Exp Mech* 55:887
- Akin JE (2005) *Finite Element Analysis with Error Estimators*. Elsevier Butterworth-Heinemann
- Donald BM (2011) *Practical stress analysis with finite elements*. Glasnevin publishing
- Bello DO, Walton S (1987) Surface topography and lubrication in sheet-metal forming. *Tribol Int* 20:59
- Grizelj B, Cumin J, Grizelj D (2013) Effect of spring back in v-tool bending of High-Strength Steel sheet metal plates. *METABK* 52:99
- Gothivarekar S, Coppieters S, Talemi RH, Debruyne D (2018) Experimental model validation and fatigue behaviour of high strength steels. *ICEM Conf. Proc*
- Lava P, Jones E, Wittevrongel L, Pierron F (2019) Validation of finite-element models using full-field experimental data: levelling FEA data through a DIC engine. *Int J Exp Mech* [under review]

Publisher's note Springer Nature remains neutral with regard to jurisdictional claims in published maps and institutional affiliations.